Contemporary Mathematics
https://ojs.wiserpub.com/index.php/CM/

Research Article

Radon-Transform-Based Similarity Measures for Non-Affine Deformable Image Registration

Rodrigo Quezada-Aguayo[1,2,3], Axel Osses[2,3], Daniel E. Hurtado[4,5*]

[1] Department of Plant Production, Faculty of Agronomy, Universidad de Concepción, Chillán, Chile
[2] Department of Mathematical Engineering, Universidad de Chile, Santiago, RM, Chile
[3] Center of Mathematical Modeling, Universidad de Chile, Santiago, RM, Chile
[4] Department of Structural and Geotechnical Engineering, School of Engineering, Pontificia Universidad Católica de Chile, Santiago, RM, Chile
[5] Institute for Biological and Medical Engineering, Pontificia Universidad Católica de Chile, Santiago, RM, Chile
E-mail: daniel.hurtado@uc.cl

Received: 28 August 2025; **Revised:** 17 October 2025; **Accepted:** 28 October 2025

Abstract: Deformable Image Registration (DIR) is a fundamental problem in biomedical imaging that analyzes organ displacements and deformations by comparing images from different states. DIR becomes particularly challenging when analyzing images that display non-affine large deformations or noisy image data. In this study, two novel similarity measures for DIR based on the Radon Transform (RT) are introduced, which, together with a linear elastic regularizer, define the formulation of the proposed projection-based DIR models. We present a theoretical analysis of the proposed RT-DIR formulation, providing conditions for the existence and uniqueness of solutions in the continuous case. The proposed RT-DIR methods are implemented using a finite-element-based deformation system and a gradient-informed quasi-Newton optimization algorithm. We compare the performance of these methods against a traditional DIR approach that employs the Sum of Squared Differences (SSD) as the similarity measure. Experimental tests include synthetic random non-affine deformations with varying noise levels and a case of real lung deformation. We show that the RT-based models exhibit enhanced accuracy in capturing non-affine deformations, higher robustness to noise, and a significantly faster convergence rate compared to the SSD-based method. We further demonstrate the applicability of the RT-DIR method on human lung images.

***Keywords*:** Deformable Image Registration (DIR), non-affine image registration, non-linear image registration, similarity measure, Radon transform, lung registration, noisy registration

MSC: 44A12, 35Q92, 65K10, 65N30, 68U10, 92C55

1. Introduction

The Deformable Image Registration (DIR) problem is a physical mathematical problem that allows the computation of the deformation field experienced by a body using two images in different states. Given two images, Reference (R) and Template (T), of a body before and after deformation, and a deformation model with desirable mechanical properties, the DIR problem can be defined as follows:

DOI: https://doi.org/10.37256/cm.6620258415

$$\text{Find } u : \Omega \subset \mathbb{R}^2 \to \mathbb{R}^2 \text{ such that } T_u := T \circ \{id + u\} \simeq R, \tag{1}$$

where Ω is the image domain and id corresponds to the identity function [1–3].

The DIR problem has been extensively utilized in the field of biomedicine for a multitude of applications, including anatomy segmentation, assisted surgery, and image fusion. These applications have been employed to analyze the diverse structures of the human body, such as different organs [4–8]. Especially in biomedicine, the DIR problem has been widely used for applications such as anatomy segmentation, assisted surgery, and image fusion, applying them to the different human organs [7]. For instance, the DIR problem has gained significant importance in recent decades due to the rising prevalence of lung diseases associated with lung stiffness. This task has presented a significant challenge due to the large and non-affine deformations that this organ exhibits. Consequently, it is imperative to develop novel DIR methods to compute large non-affine deformations, which will facilitate further technological advancement in the early detection and treatment of diseases [9–11].

Traditionally, the DIR problem has been approached using variational methods, which consist of finding the deformation field u that minimizes a cost functional given by Equation (2), where $\mathscr{D}$ is a measure of the similarity between the images R and T, $\mathscr{S}$ is a regularizer, and α is the corresponding regularization parameter [12–16]. The use of intensity-based similarity measures has become widespread in recent research due to their simplicity, speed, and the fact that they do not require segmentation [7, 17]. However, discrepancies in image intensity can occasionally cause registration challenges [11, 18]. Of particular interest is the Sum of Squared Differences (SSD) similarity measure, which is defined as the L^2 norm of the difference between images. It is a relatively simple measure to implement and has been shown to produce satisfactory results for small deformations [1].

The method employing the SSD similarity measure and a Linear Elastic Energy (LEE) regularizer has been employed in a multitude of studies to address the DIR problem [2, 19–21]. In practice, this approach is effective for capturing small deformations in noise-free images. However, a common problem with intensity-based image registration methods is that they may assume that the intensities of different pixels are independent of each other. This could lead to inefficient registration performance, especially when spatially varying intensity distortions are present [11, 18, 22]. Furthermore, this phenomenon makes intentionality-based registration methods susceptible to noise interference [11]. Consequently, SSD is less suitable for the detection of large deformations or in images with a high level of noise [23].

Registration of noisy images poses a significant challenge for intensity-based similarity measures. The presence of noise in images could result in false matches or affect gradient computation in optimization methods, potentially leading to amplified values [23, 24]. For this reason, a variety of registration methods have incorporated techniques to mitigate the effects of noise, including projection-based similarity measures, which serve to smooth out the noise in images [23–27]. Two-dimensional DIR works have incorporated projections along the rows and columns of the images in order to reduce the effects of noise in the registration process [25, 27]. Motivated by the reconstruction process that gives rise to computed-tomography images, some formulations have considered the use of the Radon transform in their similarity measures [28–30]. This approach is equivalent to finding the deformation transformation that best aligns image sinograms, rather than intensity images, which has shown great promise in reducing the effects of white noise on the registration results and method robustness [31]. In addition, intensity measures based on sinogram differences offer the possibility of developing rigid and affine registration methods using X-ray projection data directly [32–35]. Despite these advantages, the extension of registration methods based on the Radon transform to analyze images that undergo non-affine deformations has been largely overlooked. Thus, our objective is to formulate and study deformable image registration methods based on Radon-transform intensity measures.

This paper is organized as follows. In section 2, a review of the mathematical settings necessary to formulate the DIR problem is presented. The proposed DIR similarity methods based on the Radon transform are described in section 3, followed by a comprehensive analysis of the conditions for the existence and uniqueness of the solutions to the proposed DIR problems in section 4. Section 5 provides the computational considerations necessary to implement the method.

Numerical tests are presented in section 6 using several examples. Finally, section 7 discusses the strengths, scope, and limitations of the methods, as well as potential extensions of this work.

2. DIR problem

The DIR problem can be defined as the task of identifying an optimal geometric transformation, denoted by u, between two images, R and T, in different states of a given object. This transformation must satisfy the following condition: $R(x) \approx T(x+u(x))$, for all x in the image domain. Using a variational framework, the DIR problem can be formulated as follows: Given two images $R : \Omega \to \mathbb{R}$, $T : \tilde{\Omega} \to \mathbb{R}$, both in H^1, find $u : \Omega \to \mathbb{R}^2$ such that:

$$\mathscr{J}(u) := \mathscr{D}(T,\ R;\ u) + \alpha \mathscr{S}(u) \overset{u}{\to} \min, \tag{2}$$

where $\Omega \subseteq \tilde{\Omega} \subseteq \mathbb{R}^2$ are image domains, $\mathscr{D}$ is a similarity measure depending on R, T, and u; and $\mathscr{S}$ is a regularization term with regularization parameter $\alpha > 0$ [2]. It is important to ensure that the domain of T is strictly larger than the domain of R, since during the deformation process, some points in may be mapped outside of Ω. See Figure 1. In practice, when solving the DIR problem, the same image domain Ω is typically used, where $T_u : \Omega \to \mathbb{R}$, is defined by:

$$T_u(x) = \begin{cases} T(x+u(x)), & x+u(x) \in \overline{\Omega} \\ 0, & \text{otherwise.} \end{cases}$$

This implies that u can be replaced by u_M, where

$$u_M(x) = \begin{cases} u(x), & |u(x)| < M \\ u_0, & |u(x)| \geq M, \end{cases}$$

where $|u_0| = M$, for M sufficiently large (for instance $M > 2$ diam (Ω)), and therefore $T_u = T_{u_M}$.

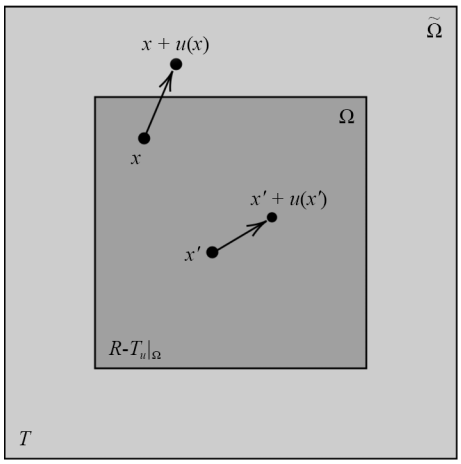

Figure 1. Diagram of domains Ω and $\tilde{\Omega}$ corresponding to the images R and T, respectively. The diagram also illustrates how a point $x \in \Omega$ can be transported by the vector field u outside the domain Ω, reaching the region $\tilde{\Omega} \setminus \Omega$

Due to its mathematical simplicity of definition and implementation, SSD is a popular choice to solve the DIR problem. The definition of SSD is as follows:

$$\mathscr{D}_{\mathrm{SSD}}(R,\ T;\ u) := \frac{1}{2}\int_{\Omega} \big(T_u(x) - R(x)\big)^2\,\mathrm{d}x, \tag{3}$$

where $R,\ T$ and u are the same as before. Similarly, the LEE regularizer is a typical choice of regularizer to solve the DIR problem. It has desirable physical properties that contribute to the solution of the DIR problem. It is defined as follows:

$$\mathscr{S}(u) := \frac{1}{2}\int_{\Omega} \mathbb{C}\,\varepsilon(u) : \varepsilon(u)\,\mathrm{d}x, \tag{4}$$

where $\varepsilon(u) := \dfrac{1}{2}\left(\nabla u + \nabla u^t\right)$ is the infinitesimal strain tensor and $\mathbb{C}$ is the elasticity tensor, that for an isotropic solid is defined by

$$\mathbb{C}\,\varepsilon := \lambda\, tr(\varepsilon)\,\mathbf{I} + 2\,\mu\,\varepsilon, \tag{5}$$

where $\lambda,\ \mu$ are the constants of Lame. The DIR method, employing the SSD similarity measure and linear elastic energy, has been examined in Barnafi et al. [13]. It was demonstrated that a solution exists under reasonable assumptions on the images.

3. Similarity measures based on the Radon transform

In this work, we introduce two variational techniques for the resolution of the DIR Problem (2) using two novel similarity measures in conjunction with the well-established LEE regularizer. In order to introduce the proposed models, it will be necessary to present some tools that will allow the definition of new similarity measures to solve the DIR problem. These tools include the Radon transform, its adjoint transform, and the sinogram. Let $\Omega = (-a,\ a)^2$, with $a > 0$. Given $f \in L^1(\Omega)$, the Radon transform of f is defined as a continuous linear operator $\mathscr{R} : L^1(\Omega) \to L^1(S^1 \times \mathbb{R})$, such that

$$\mathscr{R}(f) : [0,\ \pi] \times [-1,\ 1] \to \mathbb{R},$$

which is pointwisely defined by:

$$\mathscr{R}(f)(\omega,\ s) = \int_{\Omega} f(x)\,\delta(x\cdot\xi_{\omega} - s)\,\mathrm{d}x, \tag{6}$$

where $\xi_{\omega} = (\cos\omega, \sin\omega)$, δ is the Dirac delta and S^1 is the $1D$-semisphere.

In $2D$ dimensions, a geometric interpretation of the Radon Transform of a function f, with arguments $[\omega,\ s]$, corresponds to the integral along a straight line located according to a distance s from the origin of the coordinate system over the image domain, and at an angle $\omega^{\perp}$, counterclockwise. Furthermore, the term *sinogram* is introduced, which corresponds to a discrete visual representation of the Radon transform as an image, organized in a matrix arrangement

according to the angle θ and the distance s. In addition, the adjoint of the Radon transform of g is defined as a continuous linear operator as follows: $\mathscr{R}^{\#} : L^1(S^1 \times \mathbb{R}) \to L^1(\Omega)$, such that $\mathscr{R}^{\#}(g) : \Omega \to \mathbb{R}$ is pointwise defined by:

$$\mathscr{R}^{\#}(g)(x) := \int_{S^1} g(\theta,\, x \cdot \theta)\, \mathrm{d}\theta.$$

The interpretation of the adjoint of the Radon transform corresponds to the resultant sum of all straight line projections that passes over the point x.

It should be noted that if f is a function in the Schwartz space $S(\mathbb{R}^2)$, for example, a smooth function with compact support, then f is uniquely determined by $\mathscr{R}(f)$ [36]. It is imperative to consider this property, as it enables the definition of similarity measures that will be proposed in this work.

In this study, we propose two similarity measures. The Radon Sum of Squared Differences (RSSD) similarity is defined by:

$$\mathscr{D}_{\mathrm{RSSD}}(R,\, T;\, u) := \frac{1}{2} \int_{S^1 \times \mathbb{R}} \left(\mathscr{R}(T_u)[\xi_\omega,\, s] - \mathscr{R}(R)[\xi_\omega,\, s]\right)^2 \mathrm{d}\xi_\omega\, \mathrm{d}s, \tag{7}$$

where $\mathscr{R}$ denotes the Radon transform and $u,\ R,\ T$ are the same as before. Further, we define the Radon-Adjoint of the Radon Sum of Squared Differences ($\mathrm{R}^{\#}$RSSD) similarity as

$$\mathscr{D}_{\mathrm{R}^{\#}\mathrm{RSSD}}(R,\, T;\, u) := \frac{1}{2} \int_{\Omega} \left(\mathscr{R}^{\#}(\mathscr{R}(T_u(x))) - \mathscr{R}^{\#}(\mathscr{R}(R(x)))\right)^2 \mathrm{d}x. \tag{8}$$

It is important to note that the Radon transform of an image I, denoted by $\mathscr{R}(I)$, can be understood computationally as the sinogram of the image I. Similarly, $\mathscr{R}^{\#}(\mathscr{R}(I))$ can be understood as the back-projection of the sinogram $\mathscr{R}(I)$, also called the pseudoinverse of I. However, it is crucial to emphasise that I and $\mathscr{R}^{\#}(\mathscr{R}(I))$ are both images of the same dimension, but they are not the same image. The proposed DIR problems are as follows:

Find $u \in H^1(\Omega)$ such that:

$$\mathscr{J}_{\mathrm{RSSD}}(u) := \mathscr{D}_{\mathrm{RSSD}}(R,\, T;\, u) + \alpha_{\mathrm{RSSD}} \mathscr{S}(u) \to \min, \tag{9}$$

and,

$$\mathscr{J}_{\mathrm{R}^{\#}\mathrm{RSSD}}(u) := \mathscr{D}_{\mathrm{R}^{\#}\mathrm{RSSD}}(R,\, T;\, u) + \alpha_{\mathrm{R}^{\#}\mathrm{RSSD}} \mathscr{S}(u) \to \min, \tag{10}$$

where $\mathscr{S}$ is the LEE regularizer (4), α_{RSSD} and $\alpha_{\mathrm{R}^{\#}\mathrm{RSSD}}$ are regularization constants.

4. Conditions for the existence and uniqueness of the solution

In this section, we prove properties needed to determine the existence and uniqueness of the solution to the continuous DIR problems given in equations (9) and (10). These conditions are a direct consequence of the result presented by Barnafi et al. [13]. The authors employed the Euler-Lagrange equations to derive a weak formulation for the DIR

problem, analogous to that in Equation (2), which enabled them to determine the existence and uniqueness of solutions through the application of classical functional analysis techniques and under small data assumptions.

Definition 1 Let us define the set H as follows: $H := \{u \in H^1(\Omega) : \varepsilon(u) = 0\}^{\perp}$, with $\Omega \subset \mathbb{R}^2$.

The following lines present a summary of the theorem presented by Barnafi et al. [13].

Theorem 1 [13] Let $\mathscr{T} : H \to H$ be an operator with $\mathscr{T}(z) = u$, where for each $z \in H$, u is the solution of the problem:

Find $u \in H$ such that

$$a(u,\ v) = \hat{\alpha} F_z(v), \qquad \forall v \in H, \tag{11}$$

where $\hat{\alpha}$ is the regularization parameter associated to the DIR problem, $F_z \in H'$, and a is the continuous and non-negative bilinear form in $H^1(\Omega)$, given by

$$a(u,\ v) := \int_{\Omega} \mathbb{C}\varepsilon(u) : \varepsilon(v)\, \mathrm{d}x, \tag{12}$$

where $\mathbb{C}$ was defined in (5).

Under the following data assumptions:

H1 F_u is Lipschitz with respect to $u \in H$, *i.e.*, $\|F_u - F_v\|_{H'} \leq L_F \|u - v\|_H,\ \forall u,\ v \in H$,

H2 F_u is bounded in H', *i.e.*, $\|F_u\|_{H'} \leq M_F,\ \forall u \in H$,

then the operator $\mathscr{T}$ has at least one fixed point. Furthermore, if $\hat{\alpha} C L_F < 1$, where C is a constant coming from an *a priori* estimation given by Barnafi et al. [13, Theorem 2], the fixed point is unique.

The proof of this theorem employs a variety of tools, including Schauder's fixed point theorem, inequalities derived from the Lax-Milgram lemma and Korn's inequality, along with other standard results from functional analysis, under small data assumptions. For further details, the reader can consult the reference [13].

We note that the problems (9) and (10) can be redefined according to the formulation presented in [13]. For this, first notice that the aforementioned Problems (9) and (10) can be redefined as follows: find $u \in H^1(\Omega)$, such that:

$$\hat{\mathscr{J}}_{\mathrm{RSSD}}(u) := \mathscr{S}(u) + \hat{\alpha}_{\mathrm{RSSD}} \mathscr{D}_{\mathrm{RSSD}}(R,\ T;\ u) \to \min, \tag{13}$$

where $\hat{\alpha}_{\mathrm{RSSD}} := \dfrac{1}{\alpha_{\mathrm{RSSD}}}$, and find $u \in H^1(\Omega)$, such that:

$$\hat{\mathscr{J}}_{\mathrm{R^{\#}RSSD}}(u) := \mathscr{S}(u) + \hat{\alpha}_{\mathrm{R^{\#}RSSD}} \mathscr{D}_{\mathrm{R^{\#}RSSD}}(R,\ T;\ u) \to \min, \tag{14}$$

where $\hat{\alpha}_{\mathrm{R^{\#}RSSD}} := \dfrac{1}{\alpha_{\mathrm{R^{\#}RSSD}}}$.

The equivalence for Problem (10) is proven analogously.

Regarding the images and the solution space, let $\Omega = (-a,\ a)^2 \subset \mathbb{R}^2$ be the image domain with center $O = (0,\ 0)$, $H^1(\Omega)$ be a reasonable solution space to search for a deformation field, and R and T are two image functions in $C^2(\bar{\Omega})$, with T, and ∇T being Lipschitz and bounded functions. These Lipschitz assumptions are reasonable hypotheses according to the approximation methods described in detail in [13, p.2534].

To study the existence and uniqueness of the solutions of the proposed Problems (13) and (14), the existence and uniqueness of fixed points of the operators associated with these problems are analyzed by verifying the hypotheses **H1** and **H2** of Theorem 1, and consequently, it is verified that these fixed points are indeed local minima of the given problems.

The following lemmas present preliminary results necessary to establish the existence and uniqueness of solutions for the proposed methods required in Theorem 1. Lemma 1 establishes Lipschitz continuity properties for the images and their gradients. Lemma 2 demonstrates that the proposed models allow the formulation of the functional $F_z(v)$. Lemma 3 shows that the proposed models satisfy the necessary conditions for the existence of a fixed point, i.e., weak solutions. Theorems 2 and 3 establish sufficient conditions that guarantee the weak solutions are strong solutions.

Lemma 1 If T and ∇T are Lipschitz and bounded functions then $R - T_u$ and ∇T_u are also Lipschitz functions with respect to the variable u.

Proof. Let $u_1,\ u_2 \in H$ and $x \in \Omega$. Since T and ∇T are assumed to be Lipschitz and bounded functions, it follows that:

$$\begin{aligned} |(T_{u_1} - R)(x) - (T_{u_2} - R)(x)| &= |T(x + u_1(x)) - T(x + u_2(x))| \\ &\leq \mathrm{Lip}(T)|(x + u_1(x)) - (x + u_2(x))| \\ &\leq \mathrm{Lip}(T)|u_1(x) - u_2(x)|,\ \forall x \in \Omega\ a.e., \end{aligned} \tag{15}$$

and

$$\begin{aligned} |\nabla T_{u_1}(x) - \nabla T_{u_2}(x)| &= |\nabla T(x + u_1(x)) - \nabla T(x + u_2(x))| \\ &\leq \mathrm{Lip}(\nabla T)|(x + u_1(x)) - (x + u_2(x))| \\ &\leq \mathrm{Lip}(\nabla T)|u_1(x) - u_2(x)|,\ \forall x \in \Omega\ a.e. \end{aligned} \tag{16}$$

□

Since $R,\ T \in \mathscr{C}^2(\bar{\Omega})$, it can be shown that the Radon transforms of R and T are well defined. Consequently, the similarity measure of D_{RSSD} is well defined by (7). Using the adjoint of the Radon transform, $D_{\mathrm{R^{\#}RSSD}}$ is also well defined by (8).

In the following, the subscripts of $\hat{\mathscr{J}}_{\mathrm{RSSD}}$, $\hat{\mathscr{J}}_{\mathrm{R^{\#}RSSD}}$, $\mathscr{D}_{\mathrm{RSSD}}$, $\mathscr{D}_{\mathrm{R^{\#}RSSD}}$, $\hat{\alpha}_{\mathrm{RSSD}}$ and $\hat{\alpha}_{\mathrm{R^{\#}RSSD}}$ may be omitted. In such a case, the context will make it clear which problem is being referred to.

Lemma 2 The solutions of the Problems (13) and (14) can be written as fixed points of the equation (11), where for each $z \in H$, F_z is defined as follow:

$$F_z(v) := -\langle f_z,\ v\rangle_{L^2(\Omega)}, \quad \forall v \in H, \tag{17}$$

where f_z is the nonlinear function:

$$f_z(x) := \mathscr{R}^{\#}[\mathscr{R}(T_z - R)](x)\nabla T_z(x), \tag{18}$$

for the Problem (13), and

$$f_z(x) := \mathscr{R}^{\#}(\mathscr{R}(\mathscr{R}^{\#}[\mathscr{R}(T_z - R)]))\nabla T_z(x), \tag{19}$$

for the Problem (14).

Proof. First notice that the regularizer $\mathscr{S}(u)$ can be expressed as:

$$\mathscr{S}(u) = \frac{1}{2}a(u,\ u),$$

where a is defined in (12).

Second,

$$\mathscr{D}_{\mathrm{RSSD}}(R,\ T;\ u) = \frac{1}{2}\int_{\Omega} \mathscr{R}^{\#}[\mathscr{R}(T_u - R)](T_u - R)\,\mathrm{d}x, \tag{20}$$

whose Gateaux derivative in a direction $v \in H^1(\Omega)$ is given by:

$$D\mathscr{D}(R,\ T;\ u)[v] := \frac{d}{d\tau}\mathscr{D}(R,\ T;\ u+\tau v)\Big|_{\tau=0} = \int_{\Omega} \mathscr{R}^{\#}[\mathscr{R}(T_u - R)](x)\nabla T_u(x)\cdot v(x)\,\mathrm{d}x. \tag{21}$$

The corresponding Euler equation of the Problem (13) is

$$a(u,\ v) - \hat{\alpha}F_u(v) = 0, \quad \forall v \in H^1(\Omega), \tag{22}$$

where

$$F_u(v) = -\int_{\Omega} \mathscr{R}^{\#}[\mathscr{R}(T_u - R)](x)\nabla T_u(x)\cdot v(x)\,\mathrm{d}x, \tag{23}$$

and this is exactly (17), with $u = z$ in (18).

The analysis for Problem (14) is analogous, noting that, due to the linearity of $\mathscr{R}$ and $\mathscr{R}^{\#}$, the similarity measure (8) is equivalent to:

$$\mathscr{D}_{\mathrm{R^{\#}RSSD}}(R,\ T;\ u) = \frac{1}{2}\int_{\Omega} \mathscr{R}^{\#}(\mathscr{R}(\mathscr{R}^{\#}[\mathscr{R}(T_u - R)]))(T_u - R)\,\mathrm{d}x. \tag{24}$$

□

The following lemma proves the existence and uniqueness of the fixed points of the Problems (13) and (14), for sufficiently large regularization parameters, α_{RSSD} and $\alpha_{\mathrm{R^{\#}RSSD}}$, respectively. It is shown that the RSSD and R$^{\#}$RSSD similarity measures satisfy the necessary hypotheses of Theorem 1.

Lemma 3 The operators $\mathscr{T}$ related to the Problems (13) and (14), with $\Omega \subseteq \mathbb{R}^2$, have at least one fixed point $u \in H$. This fixed point $u \in H$ will be unique if

$$\hat{\alpha} < \frac{1}{CL_F}.$$

Proof. Since, by Lemma 1, both $T_u - R$ and $(\nabla T)_u$ are Lipschitz functions, it follows that the function f_u, defined in (18), is also Lipschitz with respect to u. Indeed, for all $u_1,\ u_2 \in H$, it has

$$
\begin{aligned}
|f_{u_1}(x) - f_{u_2}(x)| &= \left| \mathscr{R}^{\#}[\mathscr{R}(T_{u_1} - R)](x)(\nabla T)_{u_1}(x) - \mathscr{R}^{\#}[\mathscr{R}(T_{u_2} - R)](x)(\nabla T)_{u_2}(x) \right| \\
&= \Big| \left\{ \mathscr{R}^{\#}[\mathscr{R}(T_{u_1} - R)](x) - \mathscr{R}^{\#}[\mathscr{R}(T_{u_2} - R)](x) \right\} (\nabla T)_{u_1}(x) + \mathscr{R}^{\#}[\mathscr{R}(T_{u_2} - R)](x) \\
&\quad \{(\nabla T)_{u_1}(x) - (\nabla T)_{u_2}(x)\} \Big| \\
&\leq \left| \mathscr{R}^{\#}[\mathscr{R}(T_{u_2} - T_{u_1})](x) \right| |(\nabla T)_{u_1}(x)| + \left| \mathscr{R}^{\#}[\mathscr{R}(T_{u_2} - R)](x) \right| |(\nabla T)_{u_1}(x) - (\nabla T)_{u_2}(x)| \\
&\leq \left\| \mathscr{R}^{\#} \right\| \|\mathscr{R}\| \, \|(\nabla T)_{u_1}\|_{L^\infty(\Omega)} \, |T(x + u_2(x)) - T(x + u_1(x))| + \left\| \mathscr{R}^{\#} \right\| \|\mathscr{R}\| \, \|T_{u_2} - R\|_{L^\infty(\Omega)} \\
&\quad |(\nabla T)_{u_1}(x) - (\nabla T)_{u_2}(x)| \\
&\leq K_1 \mathrm{Lip}(T) |u_1(x) - u_2(x)| + K_2 \mathrm{Lip}(\nabla T) |u_1(x) - u_2(x)|, \\
&\leq [K_1 \mathrm{Lip}(T) + K_2 \mathrm{Lip}(\nabla T)] \, |u_1(x) - u_2(x)| \\
&= L_F |u_1(x) - u_2(x)|, \ \forall x \in \Omega \ a.e.,
\end{aligned}
$$

where $K_1,\ K_2$ are positive constants, such that $\|\mathscr{R}^{\#}\| \, \|\mathscr{R}\| \, \|(\nabla T)_{u_1}\|_{L^\infty(\Omega)} \leq K_1,\ \|\mathscr{R}^{\#}\| \, \|\mathscr{R}\| \, \|T_{u_2} - R\|_{L^\infty(\Omega)} \leq K_2$, and $L_F = K_1 \mathrm{Lip}(T) + K_2 \mathrm{Lip}(\nabla T)$, where $\mathrm{Lip}(T)$ and $\mathrm{Lip}(\nabla T)$ are constants given in (15) and (16). It follows that,

$$
\|f_{u_1} - f_{u_2}\|_{L^2(\Omega)} \leq L_F \|u_1 - u_2\|_{L^2(\Omega)}. \tag{25}
$$

Using (25) and Hölder's inequality, it holds that:

$$
\begin{aligned}
\|F_{u_1} - F_{u_2}\|_{H'} &= \sup_{v \in H,\ \|v\|_H \leq 1} \left| \langle f_{u_1} - f_{u_2},\ v \rangle_{L^2(\Omega)} \right| \\
&\leq \sup_{v \in H,\ \|v\|_H \leq 1} \|f_{u_1} - f_{u_2}\|_{L^2(\Omega)} \|v\|_{L^2(\Omega)} \\
&\leq \|f_{u_1} - f_{u_2}\|_{L^2(\Omega)} \sup_{v \in H,\ \|v\|_H \leq 1} \|v\|_H \\
&\leq L_F \|u_1 - u_2\|_{L^2(\Omega)},
\end{aligned}
$$

verifying the assumption **H1** of Theorem 1.

From the linearity and continuity of $\mathscr{R}$ and $\mathscr{R}^{\#}$, it follows that $\mathscr{R}^{\#}(\mathscr{R}(T_u - R))$ belongs to $L^2(\Omega)$. Hence, since $(\nabla T)_u$ and T_u were assumed to be bounded (recall that u can be replaced by u_M bounded), one finds that $f_u \in L^2(\Omega)$. Then,

$$|F_u(v)| = \left|\langle f_u,\, v\rangle_{L^2(\Omega)}\right| \leq \|f_u\|_{L^2(\Omega)}\|v\|_{L^2(\Omega)} \leq C_u\|v\|_{L^2(\Omega)} \leq C_u\|v\|_{H^1(\Omega)}, \tag{26}$$

where C_u is a continuity constant. It follows that $F_u \in (H^1(\Omega))' \subseteq H'$, verifying the assumption **H2** of Theorem 1.

Therefore, due to the Theorem 1, one obtains that $\mathscr{T}$ has at least one fixed point, and these fixed points are unique if $\hat{\alpha}CL_F < 1$. □

Since the existence of fixed points implies the existence of a solution for the weak Problem (22), in the following theorems, conditions for the existence and uniqueness of solutions for the Problems (13) and (14) are established.

Theorem 2 The Problems (13) and (14) with $\Omega \subseteq \mathbb{R}^2$, have at least one solution $u \in H$, if

$$\hat{\alpha} < \frac{K}{C_B},$$

where K is the Korn's related constant, and C_B is the same constant of (27).

This solution $u \in H$ will be unique if

$$\hat{\alpha} < \min\left\{\frac{K}{C_B},\, \frac{1}{CL_F}\right\}.$$

Proof. The existence of solutions for the weak Problem (13) is deduced due to the existence of fixed points of the operator $\mathscr{T}$, given by Lemma 3. Furthermore, it is now necessary to verify that the solutions found for Problem (22) are, in fact, minimizers for the proposed DIR Problem (13). In order to demonstrate this, it will be shown that

$$\mathrm{D}^2\,\hat{\mathscr{J}}_R(u^*)[v,\, v] > 0, \qquad \forall v \in H \setminus \{0\},$$

where u^* is the fixed point of the operator $\mathscr{T}$ found earlier, i.e., it is a solution of the weak Problem (22), with $z = u^*$.

It is known that:

$$\mathrm{D}^2\,\hat{\mathscr{J}}_R(u)[v,\, v] = \mathrm{D}^2\,\mathscr{S}(u)[v,\, v] + \hat{\alpha}\,\mathrm{D}^2\,\mathscr{D}(R,\, T;\, u)[v,\, v].$$

On the one hand, note that the derivatives of a are given by:

$$\mathrm{D}\,a(u,\, u)[v] = 2\int_\Omega \mathbb{C}\varepsilon(u) : \varepsilon(v)\,\mathrm{d}x \;\text{ and }\; \mathrm{D}^2\,a(u,\, u)[v,\, w] = 2\int_\Omega \mathbb{C}\varepsilon(w) : \varepsilon(v)\,\mathrm{d}x.$$

Additionally, from a consequence of the Poincaré inequality and from $\mathrm{trace}(\varepsilon^2(v)) = \dfrac{1}{2}|\nabla v|^2$, $\mathrm{D}^2\,a$ is coercive because:

$$\mathrm{D}^2\,a(u,\, u)[v,\, v] = 2\int_\Omega \mathbb{C}\varepsilon(v) : \varepsilon(v)\,\mathrm{d}x = 2a(v,\, v) \geq 2K\|v\|_H^2,$$

where K denotes the constant associated with the Korn inequality.

On the other hand, the first Gateaux derivative of $\mathscr{D}$ is given in (21), and its second derivative is given by:

$$\begin{aligned}
\mathrm{D}^2\,\mathscr{D}(R,\,T;\,u)[v,\,w] :&= \frac{d}{d\mu}\frac{d}{d\tau}\mathscr{D}[R,\,T;\,u+\tau v+\mu w]\Big|_{\tau=\mu=0} \\
&= \int_\Omega\ \mathscr{R}^{\#}[\mathscr{R}((\nabla T)_u\cdot v)]((\nabla T)_u\cdot w)\,\mathrm{d}x - \int_\Omega \mathscr{R}^{\#}[\mathscr{R}(R-T_u)](\mathrm{D}^2\,T)_u[v,\,w].
\end{aligned}$$

Note that, the first term of $\mathrm{D}^2\,\mathscr{D}(R,\,T;\,u)[v,\,v]$ is non-negative, because, for all $v\in H$:

$$\int_\Omega \mathscr{R}^{\#}[\mathscr{R}((\nabla T)_u\cdot v)](x)((\nabla T)_u\cdot v)(x)\,\mathrm{d}x = \int_{S^1\times\mathbb{R}}[\mathscr{R}((\nabla T)_u\cdot v)(\sigma,\,s)]^2\,\mathrm{d}\sigma\,\mathrm{d}s \geq 0.$$

Since Radon transform and its adjoint are continuous operators, $T\in C^2(\overline{\Omega})$ and R is Lipschitz, the second term of $\mathrm{D}^2\,\mathscr{D}(R,\,T;\,u)$ is bounded. For all $v\in H\setminus\{0\}$, this follows:

$$\begin{aligned}
\left|\int_\Omega \mathscr{R}^{\#}[\mathscr{R}(R-T_u)](\mathrm{D}^2\,T)_u[v,\,v]\,\mathrm{d}x\right| &\leq \int_\Omega \left|\mathscr{R}^{\#}[\mathscr{R}(R-T_u)](\mathrm{D}^2\,T)_u[v,\,v]\right|\,\mathrm{d}x \\
&\leq \|\mathscr{R}^{\#}[\mathscr{R}(R-T_u)]\|_{L^\infty(\Omega)}\int_\Omega \left|(\mathrm{D}^2\,T)_u[v,\,v]\right|\,\mathrm{d}x \\
&\leq \|\mathscr{R}^{\#}\|\,\|\mathscr{R}\|\,\|R-T_u\|_{L^\infty(\Omega)}\int_\Omega \left|(\mathrm{D}^2\,T)_u[v,\,v]\right|\,\mathrm{d}x \\
&\leq \|\mathscr{R}^{\#}\|\,\|\mathscr{R}\|\,\|R-T_u\|_{L^\infty(\Omega)}K_B\|v\|^2_{L^2(\Omega)} \\
&\leq C_B\|v\|^2_H,
\end{aligned} \tag{27}$$

where $R-T_u$ and $(\mathrm{D}^2\,T)_u$ are bounded, because u can be assumed to be bounded, and $C_B = \left\|\mathscr{R}^{\#}\right\|\,\|\mathscr{R}\|\,\|R-T_u\|_{L^\infty(\Omega)}K_B$.

Let u^* be the fixed point of the operator $\mathscr{T}$ previously found. Since $\mathrm{D}^2\,a$ is coercive, the first term of $\mathrm{D}^2\,\mathscr{D}(R,\,T;\,u)$ is positive, and the second term of $\mathrm{D}^2\,\mathscr{D}[R,\,T;\,u]$ is bounded, it follows that:

$$\begin{aligned}
\mathrm{D}^2\,\hat{\mathscr{J}}_R(u^*)[v,\,v] &= \mathrm{D}^2\,\mathscr{S}(u^*)[v,\,v] + \hat{\alpha}\,\mathrm{D}^2\,\mathscr{D}(R,\,T;\,u^*)[v,\,v] \\
&= \frac{1}{2}\,\mathrm{D}^2\,a(u^*,\,u^*)[v,\,v] + \hat{\alpha}\,\mathrm{D}^2\,\mathscr{D}(R,\,T;\,u^*)[v,\,v] \\
&\geq K\|v\|^2_H + \hat{\alpha}\int_\Omega \mathscr{R}^{\#}[\mathscr{R}((\nabla T)_{u^*}\cdot v)]((\nabla T)_{u^*}\cdot v)\,\mathrm{d}x
\end{aligned}$$

$$- \hat{\alpha} \int_{\Omega} \mathscr{R}^{\#}[\mathscr{R}(T_{u^*} - R)](\mathrm{D}^2 T)_{u^*}[v,\ v]\,\mathrm{d}x$$

$$\geq K\|v\|_H^2 + \underbrace{\hat{\alpha} \int_{\Omega} [\mathscr{R}(\,(\nabla T)_{u^*} \cdot v)]^2\,\mathrm{d}x}_{\geq 0} - \hat{\alpha} C_B \|v\|_H^2$$

$$\geq (K - \hat{\alpha} C_B)\|v\|_H^2.$$

And, by imposing that $\hat{\alpha} < \dfrac{K}{C_B}$,

$$\mathrm{D}^2\, \hat{\mathscr{J}}_R(u^*)[v,\ v] > 0.$$

From the continuity of the functional $\hat{\mathscr{J}}_R$ and the fact that $\mathrm{D}^2\, \hat{\mathscr{J}}_R(u^*)[v,\ v] > 0$, it follows that u^* is also a local minimum of $\hat{\mathscr{J}}_R$ if $\hat{\alpha} < \dfrac{K}{C_B}$. And, in accordance with the Lemma 3, this solution u^* will be unique if

$$\hat{\alpha} < \min\left\{ \frac{K}{C_B},\ \frac{1}{CL_F} \right\}.$$

The proof of the previous result for the Problem (14) is also analogous. □

In addition, to prove that u^* is the minimum of the functional $\hat{\mathscr{J}}_R$, an alternative demonstration using a Taylor expansion is included. The idea is to show that $\hat{\mathscr{J}}_R$ is a convex functional around u^*, i.e., for all directions $v \in H$ it holds that $\hat{\mathscr{J}}_R[u^* + v] > \hat{\mathscr{J}}_R[u^*]$.

Theorem 3 The Problems (13) and (14) with $\Omega \subseteq \mathbb{R}^2$, have at least a solution $u \in H$ if $\hat{\alpha} < \dfrac{C_{coe}}{2C_{BC}}$, where C_{coe} is a coercivity constant and C_{BC} is a continuity constant. This solution $u \in H$ will be unique if

$$\hat{\alpha} < \min\left\{ \frac{C_{coe}}{2C_{BC}},\ \frac{1}{CL_F} \right\}.$$

Proof. Due to the existence of fixed points of the operator $\mathscr{T}$, given by Lemma 3, the existence of solutions for the weak Problem (13) is deduced. Furthermore, it must be verified that the fixed points found for (22) are indeed minimizers for the proposed DIR Problem (13).

Let $v \in H \setminus \{0\}$ be an arbitrary direction. Given the u^* solution to Problem (22), it follows that $a(u^*,\ v) - \hat{\alpha} F_{u^*}(v) = 0$. Furthermore, from the symmetry and positively of the bilinear form a, and a Taylor expansion of $\mathscr{D}[R,\ T;\ u]$ at u^* in the direction v, one obtains that:

$$\hat{\mathscr{J}}_R[u^* + v] := \mathscr{S}[u^* + v] + \hat{\alpha}\mathscr{D}[R,\ T;\ u^* + v]$$

$$= \frac{1}{2}a(u^*,\ u^*) + a(u^*,\ v) + \frac{1}{2}a(v,\ v) + \hat{\alpha}\{\mathscr{D}[R,\ T;\ u^*]$$

$$+ \nabla\mathscr{D}[R,\ T;\ u^*] \cdot v + r_{u^*,\,2}(v)\}$$

$$= \left\{\frac{1}{2}a(u^*,\ u^*) + \hat{\alpha}\mathscr{D}[R,\ T;\ u^*]\right\} + \left\{a(u^*,\ v) - (-\hat{\alpha}\nabla\mathscr{D}[R,\ T;\ u^*]\cdot v)\right\}$$

$$+ \frac{1}{2}a(v,\ v) + \hat{\alpha}r_{u^*,\,2}(v)$$

$$= \hat{\mathscr{J}}_R[u^*] + \{\underbrace{a(u^*,\ v) - \hat{\alpha}F_{u^*}(v)}_{=0}\} + \frac{1}{2}a(v,\ v) + \hat{\alpha}r_{u^*,\,2}(v)$$

$$= \hat{\mathscr{J}}_R[u^*] + \frac{1}{2}a(v,\ v) + \hat{\alpha}r_{u^*,\,2}(v),$$

where $r_{u^*,\,2}(v) := \frac{1}{2}\mathrm{D}^2\,\mathscr{D}[R,\ T;\ u^* + cv][v,\ v]$ is the remainder, with $c \in (0,\ 1)$. Let $\hat{\alpha} > 0$ and $a(v,\ v) > 0$. If $r_{u^*,\,2}(v) \geq 0$, then $\hat{\mathscr{J}}_R[u^* + v] > \hat{\mathscr{J}}_R[u^*]$. If $r_{u^*,\,2}(v) < 0$, it is necessary that:

$$\hat{\alpha} < \frac{a(v,\ v)}{|2r_{u^*,\,2}(v)|}, \quad \forall v \in H. \tag{28}$$

Since a is coercive, there exists C_{coe} such that $a(v,\ v) \geq C_{coe}\|v\|^2$. And since the expression $\mathrm{D}^2\,\mathscr{D}[R,\ T;\ u^* + cv][\cdot,\ \cdot]$ is a continuous bilinear form, there exist $C_{BC} > 0$, such that:

$$|r_{u^*,\,2}| \leq \left|\frac{1}{2}\mathrm{D}^2\,\mathscr{D}[R,\ T;\ u^* + cv][v,\ v]\right| \leq C_{BC}\|v\|^2.$$

So if we take $\hat{\alpha} < \dfrac{C_{coe}}{2C_{BC}}$, it follows:

$$\left|\frac{a(v,\ v)}{2r_{u^*,\,2}(v)}\right| \geq \frac{C_{coe}\|v\|^2}{C_{BC}\|v\|^2} \geq \frac{C_{coe}}{C_{BC}} > \hat{\alpha}. \tag{29}$$

It can thus be concluded that if the condition $\hat{\alpha} < \dfrac{C_{coe}}{2C_{BC}}$ is satisfied, the fixed point u^* is also a local minimum of $\hat{\mathscr{J}}_R$. And, in accordance with the Lemma 3, this solution u^* will be unique if

$$\hat{\alpha} < \min\left\{\frac{C_{coe}}{2C_{BC}},\ \frac{1}{CL_F}\right\}.$$

The proof of the previous result for the Problem (14) is also analogous. □

It should be noted that the results previously obtained for the reformulated Problems (13) and (14) are also applicable to the Problems (9) and (10).

5. Numerical implementation

To numerically solve DIR problems (9) and (10), we develop a finite-element formulation. Let $\mathscr{V} = H^1(\Omega)$ and let $\Omega^h \subset \Omega$ be the image domain composed by elements Ω^e satisfying that $\Omega^h = \cup_{e=1}^{n_{el}} \Omega^e$. Based on this domain discretization, we construct the finite-element space $\mathscr{V}^h \subset \mathscr{V}$ as

$$\mathscr{V}^h := \left\{ u^h \in \mathscr{V} \,|\, u^h(x) = \sum_{A=1}^{N_{dof}} N_A(x) u_A \right\},$$

where N_{dof} is the number of degrees of freedom, $\{N_A(x) : A = 1, \cdots, N_{dof}\}$ is the set of shape (basis) functions and u_A are the nodal displacements of the vertices x_A of the elements in the domain Ω^h. The N_A functions satisfy the Kronecker delta identity in the nodes, *i.e.*, $N_A(x^B) = \delta_{AB}$. In what follows, we will consider shape functions based on continuous piecewise-linear polynomials over the domain Ω^h.

The deformation field $u \in \mathscr{V}$ can be approximated by an element $u^h \in \mathscr{V}^h$ which satisfies:

$$u(x) \approx u^h(x) := \sum_{A=1}^{N_{dof}} N_A(x) u_A,$$

where all vertices have free motion, including the nodes at the edges of the image.

For the calculation of the deformations, two triangular Delaunay meshes were considered, as shown in Figure 2. A *coarse* mesh with 64 elements, 41 nodes, and 82 degrees of freedom, and a *fine* triangular mesh with 545 elements, 1,024 nodes and 2,048 degrees of freedom.

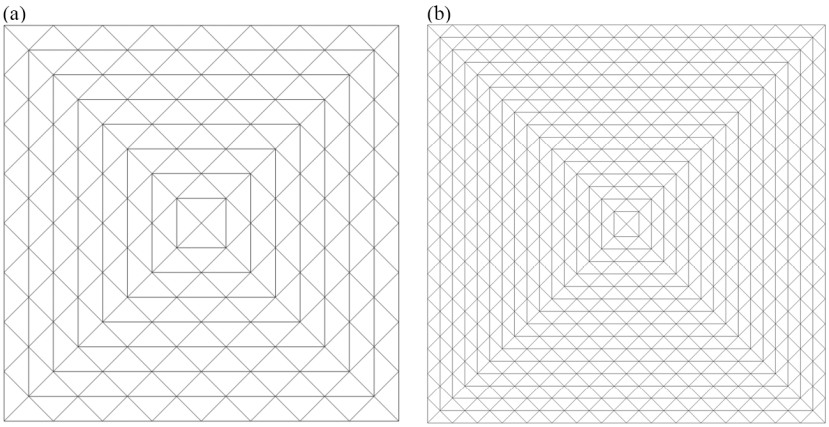

Figure 2. Delaunay meshes utilized for experiments

The discretization of the LEE regularizer (4) leads to the quadratic form

$$\mathscr{S}^h(u^h) := \mathbf{u}^t \mathbf{K} \mathbf{u}, \tag{30}$$

where $\mathbf{u} = (u_{A_1}, \cdots, u_{A_{N_{dof}}})$, and $\mathbf{K}$ is the stiffness matrix, computed by $K := \int_{\Omega^h} B_A^T D B_A \, \mathrm{d}\Omega^h$, where D is the Cauchy tensor, B is an array representing the term $\varepsilon(N_A(x))$ in equation (4), $N_{A,\,1}$ and $N_{A,\,2}$ are the derivatives of the Finite Element Method (FEM) basis function, and

$$B_A^T := \begin{bmatrix} N_{A,\,1} & 0 & N_{A,\,2} \\ 0 & N_{A,\,2} & N_{A,\,1} \end{bmatrix}.$$

For details, see [37, Sections 2.7-2.9].

The similarity measure $\mathscr{D}_{SSD}$ is discretized as follows:

$$\mathscr{D}_{SSD}^h(R,\, T;\, u) := \frac{4}{N^2} \|R - T_{u^h}\|_2^2,$$

where $u^h \in \mathscr{V}^h$ is the deformation field, R and T_{u^h} are images of size $N \times N$, T_{u^h} is the interpolated image which takes the intensities of T in the pixel $(i,\, j)$, and assigns them to the pixel $(i,\, j) + u^h$.

The similarity measure $\mathscr{D}_{\mathrm{RSSD}}$ is discretized as:

$$\mathscr{D}_{\mathrm{RSSD}}^h[R,\, T;\, u^h] := \frac{1}{2} \cdot \frac{2\pi}{N_\omega N_s} \sum_{\omega=1}^{N_\omega} \sum_{s=1}^{N_s} \big(\mathscr{R}\big(T_{u^h}\big)[\omega,\, s] - \mathscr{R}(R)[\omega,\, s]\big)^2, \tag{31}$$

where $N \times N$ pixels, N_ω is the number of equidistant nodes in $[0,\, \pi]$, N_s is the number of equidistant nodes in $[-1,\, 1]$, and where u^h, R and T_{u^h} are the same as before.

From the linearity of the Radon transform, D_{RSSD}^h is calculated directly from the sinograms of the images R and T_u^h, as follows:

$$\mathscr{D}_{\mathrm{RSSD}}^h[R,\, T;\, u^h] = \frac{1}{2} \cdot \frac{2\pi}{N_\omega N_s} \|\mathrm{sinogram}(T_{u^h}) - \mathrm{sinogram}(R)\|^2, \tag{32}$$

where sinogram (R) and sinogram (T_{u^h}) are real matrix of size $N_s \times N_\omega$.

The similarity measure $\mathscr{D}_{\mathrm{R}^\#\mathrm{RSSD}}$ is discretized as:

$$\mathscr{D}_{\mathrm{R}^\#\mathrm{RSSD}}^h[R,\, T;\, u^h] := \frac{1}{2} \cdot \frac{4}{N^2} \sum_{i,\, j=1}^{N} \big(\mathscr{R}^\#(\mathscr{R}\big(T_{u^h}\big))(i,\, j) - \mathscr{R}^\#(\mathscr{R}(R))(i,\, j)\big)^2 \tag{33}$$

where u^h, R, T, T_{u^h} and N are the same as before.

The term $D_{\mathrm{R}^\#\mathrm{RSSD}}^h$ can be calculated directly from the sinograms of R and T_u^h, as follows:

$$\mathscr{D}_{\mathrm{R}^\#\mathrm{RSSD}}^h[R,\, T;\, u^h] = \frac{1}{2} \cdot \frac{4}{N^2} \|\text{Back-Projection (BP) (sinogram } (T_{u^h})) - \text{BP (sinogram } (R))\|^2, \tag{34}$$

where BP (sinogram (T_{u^h})) and BP (sinogram (R)) represent real matrices of size $N \times N$, corresponding to the back-projection of the sinograms. Accordingly, the functionals $\mathscr{J}_{\mathrm{RSSD}}[u]$ and $\mathscr{J}_{\mathrm{R}^\#\mathrm{RSSD}}[u]$ can be discretized. Since the measures $\mathscr{D}_{SSD}^h$, $\mathscr{D}_{\mathrm{RSSD}}^h$ and $\mathscr{D}_{\mathrm{R}^\#\mathrm{RSSD}}^h$ have different ranges and are dissimilar, scaling adjustment factors were been

integrated into the similarity measures. This enables the regularization parameters of the three models to be set within a narrow range. It is noteworthy that these modifications do not affect the effectiveness of the methods.

In terms of images and sinograms, the following experiments use grayscale images of size 128×128 pixels, with intensities in the range $[0,\ 1]$, and with image domain $\Omega = [-1,\ 1]^2$. To discretize the Radon transform, the variable s was considered to be in the interval $[-1,\ 1]$, with 185 equidistant distances, while the variable ω was considered to be in the interval $[0,\ \pi]$, with 360 equidistant angles. Consequently, the values of h_s and h_ω are given by $2/128$ and $\pi/180$, respectively.

The numerical computations are done using the MATLAB R2022B software. The radon script function is used to construct the sinograms. Subsequently, the back projection of the sinograms is constructed using the iradon script function with the configuration filter = none.

To minimize the DIR problem, two existing MATLAB programs are employed: The optimization algorithms used are fminunc and fmincon. By default, the first uses a quasi-newton-type, and the second uses an algorithm of type interior-point type. Both methods use algorithms of type Broyden-Fletcher-Goldfarb-Shanno (BFGS) for the Hessian update. Furthermore, to improve the methodology, the analytical gradient of both functionals has been incorporated. Using the previously introduced notation, components of the gradient of the objective functions $\mathscr{J}^h_{\mathrm{SSD}}$, $\mathscr{J}^h_{\mathrm{RSSD}}$, and $\mathscr{J}^h_{\mathscr{R}^{\#}\mathrm{RSSD}}$ with respect to a node u_A, respectively, were computed as follows:

$$\frac{\partial}{\partial u_A}\mathscr{J}_{\mathrm{SSD}}[u^h] = \frac{4}{N}\sum_{i,\ j=1}^{N}[R - T_{u^h}]\left[-\frac{\partial}{\partial u_A}(T_{u^h})N_A\right] + \alpha K\mathbf{u},$$

$$\frac{\partial}{\partial u_A}\mathscr{J}_{\mathrm{RSSD}}[u^h] = \frac{2\pi}{N_\omega N_s}\sum_{\omega^h=1}^{N_\omega}\sum_{s^h=1}^{N_s}\mathscr{R}[R - T_{u^h}]\mathscr{R}\left[-\frac{\partial}{\partial u_A}(T_{u^h})N_A\right] + \alpha K\mathbf{u},$$

$$\frac{\partial}{\partial u_A}\mathscr{J}_{\mathscr{R}^{\#}\mathrm{RSSD}}[u^h] = \frac{4}{N}\sum_{i,\ j=1}^{N}\sum_{i,\ j=1}^{N}\mathscr{R}^{\#}\mathscr{R}[R - T_{u^h}]\mathscr{R}^{\#}\mathscr{R}\left[-\frac{\partial}{\partial u_A}(T_{u^h})N_A\right] + \alpha K\mathbf{u},$$

were $\mathscr{R}$ and $\mathscr{R}^{\#}$ were computed as mentioned before, and $\dfrac{\partial}{\partial u_A}(T_{u^h})$ was computed using a centered finite difference scheme. The sinograms and the back-projections were used in the same way as before.

We considered two error metrics to assess the performance of all registration methods studied in this work. Let $R,\ T$ be two images with size $N \times N$. Then, the Root Mean Square Error (RMSE) is defined as the norm between the difference of these two images, namely

$$\mathrm{RMSE}(R,\ T) := \sqrt{\frac{1}{N^2}\sum_{i,\ j=1}^{N}(R_{ij} - T_{ij})^2},$$

where R_{ij} and T_{ij} are the pixels at position $(i,\ j)$. An RMSE value equal to zero indicates that both images are identical.

Let $u,\ v \in L^2(\Omega,\ \mathbb{R}^2)$. We consider the L^2-error given by

$$L^2\text{-error}(u,\ v) := \left(\int_\omega \left\{(u_1 - v_1)^2 + (u_2 - v_2)^2\right\}\right)^{1/2}$$

where u_i and v_i are the i-th component of vector fields u and v, respectively. A value of this index in close proximity to zero indicates that the registration calculated by the method is an accurate approximation of the ground-truth deformation field.

6. Model calibration and registration of noisy phantoms and lung images

6.1 *Parameter calibration using synthetic images and k-fold cross validation*

Thirty pairs of (R, T) noise-free images were generated to create a dataset for training and validation. The reference image R for all pairs was the Shep-Logam phantom image. Target images were generated from applying non-affine transformations on the reference image R. The non-affine transformation consisted of a global affine deformation with nonhomogeneous scaling in the principal directions, using values randomly sampled from the interval $[0.69, 0.91]$. Then, a random rotation within the interval $[-30°, 30°]$ was applied. In addition, a nodal translation of up to nine pixels in random directions was applied, creating a non-affine deformation field. Figure 3 illustrates a subset of the generated template images, which display non-affine transformations of the Reference image R.

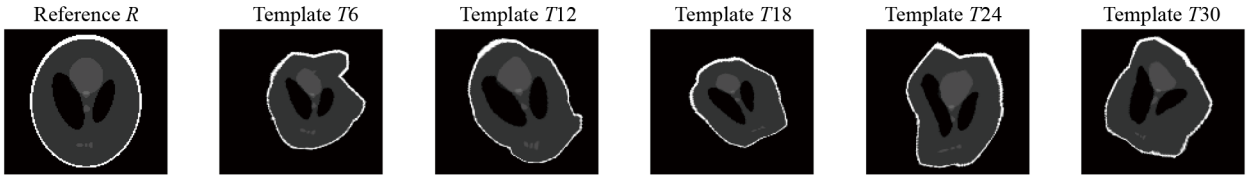

Figure 3. Reference (R) and selected synthetic template images ($T6$, $T12$, $T18$, $T24$, $T30$) from the 30-image dataset used to calibrate the regularization parameter and to evaluate the performance of registration methods

To determine the regularization parameter α in an unbiased way, we employed a k-fold cross-validation procedure [38]. To this end, the 30-image dataset was partitioned into $k = 6$ groups of 5 images each, randomly assigned during each split. One randomly selected group was assigned as the test dataset, while the other 5 groups were used as the training dataset. Then, for each group, the regularization parameter α was found by minimizing the cost function through a grid search on the sampling space $\alpha \in [0.0001, 0.001]$.

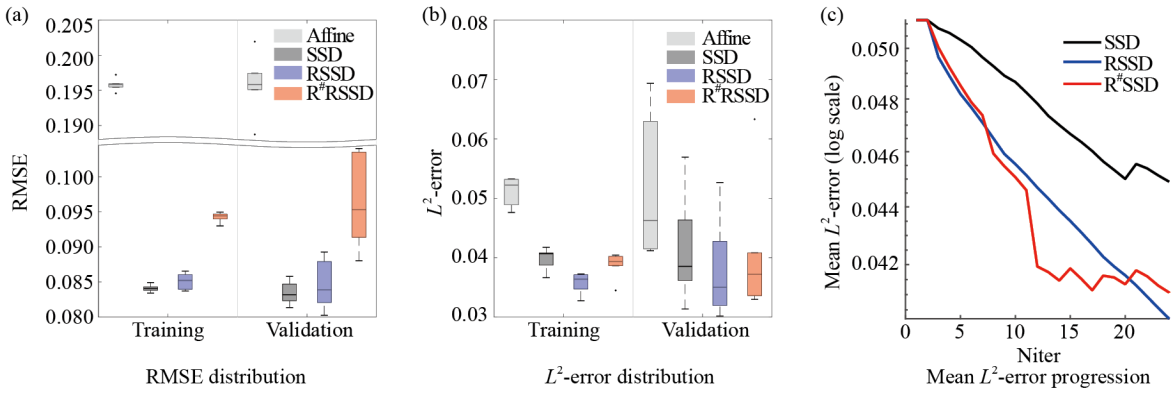

Figure 4. Performance analysis and comparison for the Affine, SSD, RSSD, and R$^{\#}$SSD methods. (a) RMSE distributions associated with the training and testing datasets, (b) L^2-error distributions associated with the training and testing datasets, (c) progression of the mean L^2-error during the numerical optimization of registration methods

The resulting regularization parameters were $\alpha_{SSD} = 0.005 \pm 0.0001$, $\alpha_{\text{RSSD}} = 0.003 \pm 0.004$, and $\alpha_{\text{R}^{\#}\text{RSSD}} = 0.0006 \pm 0.001$. Figures 4a and 4b report the distributions of the Affine, SSD, RSSD, and R$^{\#}$SSD methods for the RMSE

and L^2-error metrics, respectively. During both the training and validation steps, the Affine method resulted in larger errors than the other methods. Figure 4c reports the progression of the L^2-error during the optimization process of the SSD, RSSD, and R$^{\#}$SSD methods, all of which displayed a decreasing trend as the iterations increased.

6.2 *Registration of noisy synthetic images undergoing non-affine deformation fields*

To study the effect of noise on the performance of registration methods, we applied a random Gaussian noise to the 30-image dataset described above. Two levels of noise were considered: a *low noise* of type white Gaussian with mean 0 and variance 0.05^2 and a *high noise* of type white Gaussian with mean 0 and variance 0.1^2.

Figures 5a and 5b show a comparison of the performance of the Affine, SSD, RSSD, and R$^{\#}$SSD methods when registering the 30-image noisy datasets measured in terms of the RMSE and L^2-error, respectively. Regardless of the noise level, the Affine method consistently delivered higher RMSE and L^2-error values than the other registration methods. The RSSD method yielded the best performance for both noise levels when measuring differences in image intensities, as indicated by the RMSE.

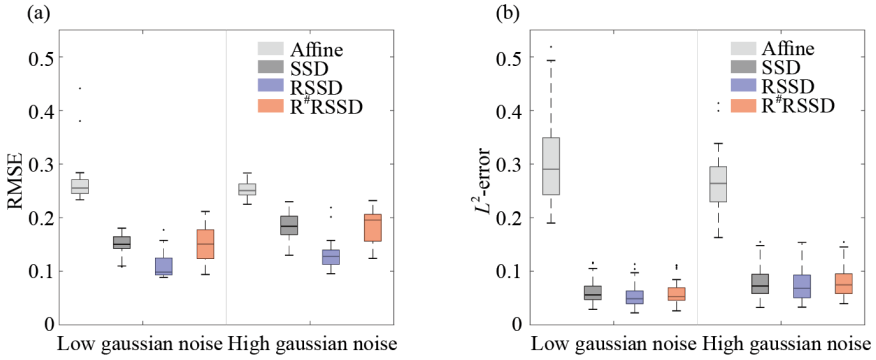

Figure 5. Performance analysis of registration methods under two levels of noise using a 30-image dataset

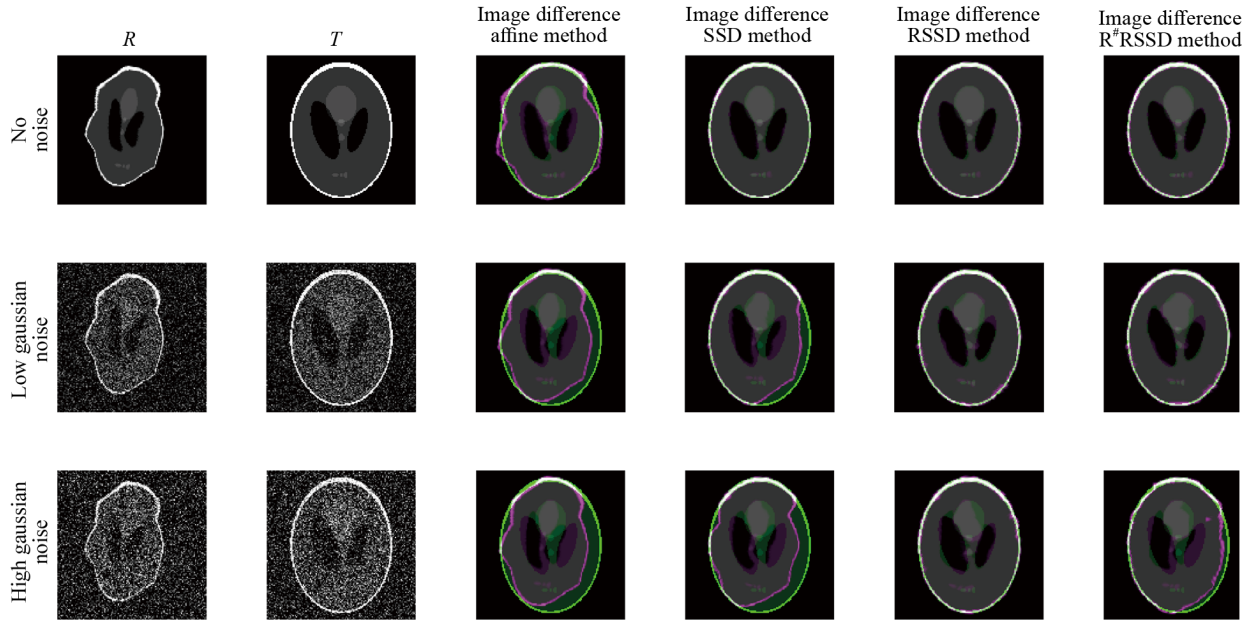

Figure 6. Reference, Target, and Difference Images for the different registration methods considered in this study for the case of image dataset 8. Rows correspond to different levels of noise applied to the synthetic image. Overall, the RSSD method delivered the best difference image for this case

Figure 6 offers a graphical analysis of the performance of all four registration methods when applied to case 8 of the image dataset subject to increasing levels of noise. Visually, the RSSD method resulted in the best match between the Reference and the composed Target images, which were not affected by noise.

Figures 7a and 7b report the L^2-error evolution of the deformation field during numerical optimization for the three registration methods applied to the low and high-noise 30-image datasets. For the low-noise case, all registration methods delivered successive solutions that reduced the L^2-error as iterations increased. For the high-noise case, only the SSD method provided a sequence of solutions that decreased the L^2-error as iterations increased. For the SSD and R$^{\#}$SSD methods, the L^2-error increased during the optimization process.

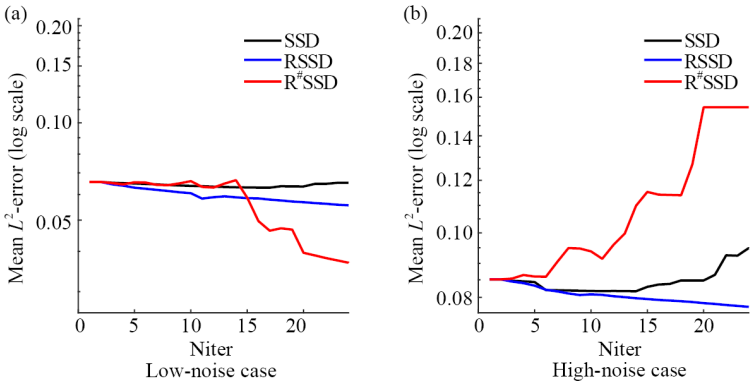

Figure 7. Evolution of the deformation field error during numerical optimization when registering the 30-image dataset with the SSD, RSSD, and R$^{\#}$RSSD methods: (a) low-noise case, and (b) high-noise case. Lines represent the mean L^2-error of the deformation field for each iteration

6.3 *Registration of computed-tomography lung images*

To demonstrate the applicability of the methods proposed in this work, we analyzed a set of computed tomography images from human lungs reported in a previous study [39]. Figure 8a and 8b show the Reference and Target images, respectively. Figure 8c shows the difference between these two images, which evidences how different the lung shapes are before image registration. Figures 8d, 8e, 8f show the results of applying the SSD, RSSD, and R$^{\#}$RSSD registration methods, respectively. The RSSD delivers the best match between Reference and Registered Target images, followed by the R$^{\#}$RSSD. The SSD method resulted in a registered image that achieves some overlap on the top part of the lungs, but does not capture the motion observed in the bottom part of the lungs (diaphragmatic region).

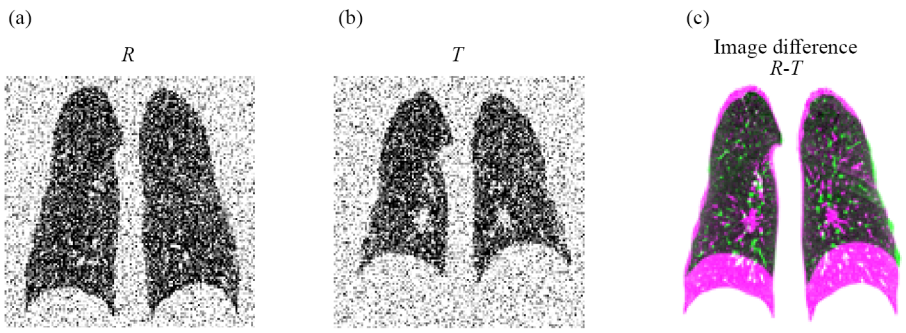

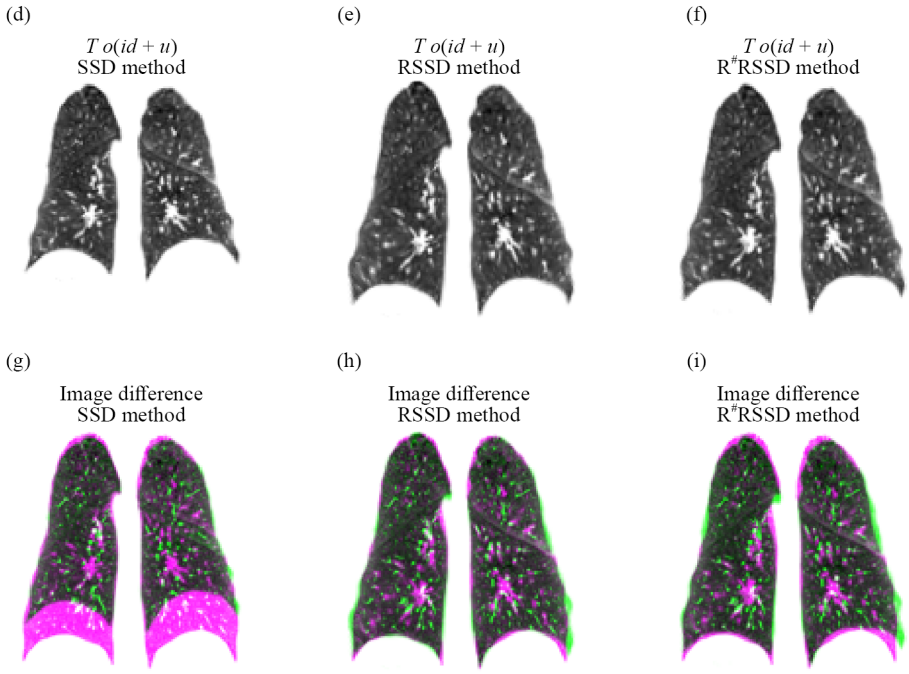

Figure 8. DIR of noisy lung images. (a) Reference image, (b) Target image, (c) Image difference before registration, (d) SSD registration image, (e) RSSD registration image, (f) $R^{\#}$RSSD registration image, (g) Image difference after SSD registration, (h) Image difference after RSSD registration, (i) Image difference after $R^{\#}$RSSD registration

7. Discussion and conclusions

In this work, we propose, analyze, and evaluate DIR methods based on two novel similarity measures, RSSD and $R^{\#}$SSD, both of which incorporate the Radon transform in their formulation.

From a mathematical perspective, we offer a formal analysis of the proposed DIR methods, establishing conditions on the model parameters that guarantee the existence and uniqueness of strong solutions. This result extends what has been previously demonstrated in formulations based on SSD intensity measures, which only provide conditions for the existence of weak solutions [13]. Our contribution also extends the results reported for sinogram-based DIR approaches, which were restricted to affine deformation models and do not prove the existence and uniqueness of solutions [24–28].

From a numerical point of view, we assessed the performance of the proposed methods and compared them to state-of-the-art affine and non-affine registration methods by analyzing synthetic images with varying levels of deformation and noise. Under all of the error metrics considered, the Affine method always resulted in higher error values than the SSD, RSSD; and $R^{\#}$SSD methods, see Figures 4 and 5. This is to be expected, as the transformations applied to the synthetic reference images were strongly non-affine (Figure 3), justifying the use of registration methods that could handle non-affine numerical representations. Interestingly, the SSD method provided a robust approach to handling image noise, delivering the best registration solution among all methods studied for the noise levels considered, see Figures 5 and 6. Increasing the noise level markedly affected the solution provided by the SSD and $R^{\#}$SSD methods, as the deformation field error of solutions delivered by those methods increased during numerical optimization, despite the fact that successive iterations decreased their cost functions.

We demonstrated the applicability of the proposed methods by registering medical images of human lungs. Our results show that the RSSD method provides a highly acceptable registered image when compared to the Reference image, see Figure 8. In particular, the resulting deformation field is capable of accommodating small deformations in the upper lung domain and large deformations in the regions close to the lung diaphragm [40]. The pattern observed in the lung deformation field is consistent with the results from studies that specifically assess deformation in lungs from medical

images [5]. These results confirm the advantage of considering similarity measures based on the Radon Transform in the development of DIR methods that target images with high levels of noise [31, 41].

Our work can benefit from many improvements that offer opportunities for future work. First, we note that we did not analyze the spatial convergence of our results as the mesh size is reduced. Future contributions could consider a sequence of subsequently finer discretizations to study how finer meshes improve the registration results [13]. Another interesting avenue of research is to consider adaptive meshing schemes for the spatial discretization of the proposed similarity measures, which have been shown to be more efficient in numerical terms [42–44]. The use of Gaussian noise to evaluate the robustness of the analyzed methods against noise also constitutes a limitation of this work. We remark that medical images can be subject to non-Gaussian noise. Future work should assess the effectiveness of the proposed registration methods when applied to images affected by non-Gaussian noise. Finally, the extension of the proposed methods for the analysis of 3D images remains an important development necessary for bridging these methods into medical applications [34].

Acknowledgments

Rodrigo Quezada is grateful for the support from ANID BECAS/DOCTORADO NACIONAL/2016-21160751. Axel Osses acknowledges funding from ANID-Fondecyt 1240200, 1231404, CMM FB210005 Basal-ANID, FONDAP 1523A0002, ECOS 240038, FONDEF IT23I0095 and DO ANID Technology Center DO210001. Daniel E. Hurtado acknowledges the support of ANID Chile through grant Fondecyt Regular #1220465.

Conflict of interest

The authors declare no competing financial interest.

References

[1] Goshtasby AA. *Image Registration: Principles, Tools and Methods*. London, UK: Springer Science & Business Media; 2012.

[2] Modersitzki J. *Numerical Methods for Image Registration*. Oxford: Oxford University Press on Demand; 2004.

[3] Ruthotto L, Modersitzki J. Non-linear image registration. In: *Handbook of Mathematical Methods in Imaging*. New York: Springer; 2015. p.2005-2051.

[4] Bathina YB, Medathati MK, Sivaswamy J. Robust matching of multi-modal retinal images using radon transform based local descriptor. In: *Proceedings of the 1st ACM International Health Informatics Symposium*. Hyderabad, India: ACM Press; 2010. p.765-770.

[5] Hurtado DE, Villarroel N, Andrade C, Retamal J, Bugedo G, Bruhn A. Spatial patterns and frequency distributions of regional deformation in the healthy human lung. *Biomechanics and Modeling in Mechanobiology*. 2017; 16(4): 1413-1423.

[6] Ferrant M, Nabavi A, Macq B, Black PM, Jolesz FA, Kikinis R, et al. Serial registration of intraoperative MR images of the brain. *Medical Image Analysis*. 2002; 6(4): 337-359.

[7] Oliveira FPM, Tavares JMRS. Medical image registration: A review. *Computer Methods in Biomechanics and Biomedical Engineering*. 2014; 17(2): 73-93.

[8] Schnabel JA, Tanner C, Castellano-Smith AD, Degenhard A, Leach MO, Hose DR, et al. Validation of nonrigid image registration using finite-element methods: Application to breast MR images. *IEEE Transactions on Medical Imaging*. 2003; 22(2): 238-247.

[9] Cruces P, Erranz B, Lillo F, Sarabia-Vallejos MA, Iturrieta P, Morales F, et al. Mapping regional strain in anesthetised healthy subjects during spontaneous ventilation. *BMJ Open Respiratory Research*. 2019; 6(1): e000423.

[10] Retamal J, Hurtado D, Villarroel N, Bruhn A, Bugedo G, Amato MBP, et al. Does regional lung strain correlate with regional inflammation in acute respiratory distress syndrome during nonprotective ventilation? An experimental porcine study. *Critical Care Medicine*. 2018; 46(6): e591-e599.

[11] Xing L, Liu W, Wang X, Li X, Xu R, Wang MH. Deformable registration network based on multi-scale features and cumulative optimization for medical image alignment. *Biomedical Signal Processing and Control*. 2024; 95: 106172.

[12] Aubert G, Kornprobst P. *Mathematical Problems in Image Processing: Partial Differential Equations and the Calculus of Variations*. 2nd ed. New York: Springer Science & Business Media; 2006.

[13] Barnafi N, Gatica GN, Hurtado DE. Primal and mixed finite element methods for deformable image registration problems. *SIAM Journal on Imaging Sciences*. 2018; 11(4): 2529-2567.

[14] Chen C, Oktem O. Indirect image registration with large diffeomorphic deformations. *SIAM Journal on Imaging Sciences*. 2018; 11(1): 575-617.

[15] Oektem O, Chen C, Domanic NO, Ravikumar P, Bajaj C. Shape-based image reconstruction using linearized deformations. *Inverse Problems*. 2017; 33(3): 035004.

[16] Vese LA, Le Guyader C. *Variational Methods in Image Processing*. Boca Raton, FL, USA: CRC Press; 2016.

[17] Maintz JBA, Viergever MA. A survey of medical image registration. *Medical Image Analysis*. 1998; 2(1): 1-36.

[18] Aghajani K, Yousefpour R, Shirpour M, Manzuri MT. Intensity based image registration by minimizing the complexity of weighted subtraction under illumination changes. *Biomedical Signal Processing and Control*. 2016; 25: 35-45.

[19] Ashburner J, Friston KJ. Nonlinear spatial normalization using basis functions. *Human Brain Mapping*. 1999; 7(4): 254-266.

[20] Brown LG. A survey of image registration techniques. *ACM Computing Surveys (CSUR)*. 1992; 24(4): 325-376.

[21] Capek K. Optimisation strategies applied to global similarity based image registration methods. In: *International Conferences in Central Europe on Computer Graphics, Visualization and Computer Vision (WSCG)*. Plzen, Czech Republic: WSCG; 1999. p.369-374.

[22] Shirpour M, Aghajani K, Manzuri-Shalmani M. A new similarity measure for intensity-based image registration. In: *2014 4th International Conference on Computer and Knowledge Engineering (ICCKE)*. Mashhad, Iran: IEEE; 2014. p.227-232.

[23] Bajcsy R, Kovačič S. Multiresolution elastic matching. *Computer Vision, Graphics, and Image Processing*. 1989; 46(1): 1-21.

[24] Cain SC, Hayat MM, Armstrong EE. Projection-based image registration in the presence of fixed-pattern noise. *IEEE Transactions on Image Processing*. 2001; 10(12): 1860-1872.

[25] Albu F, Corcoran P. Transformed integral projection method for global alignment of second order radially distorted images. In: *2014 Signal Processing: Algorithms, Architectures, Arrangements, and Applications (SPA)*. Poland: IEEE; 2014. p.42-47.

[26] Khamene A, Chisu R, Wein W, Navab N, Sauer F. A novel projection based approach for medical image registration. In: *International Workshop on Biomedical Image Registration*. Berlin, Heidelberg: Springer; 2006. p.247-256.

[27] Sauer K, Schwartz B. Efficient block motion estimation using integral projections. *IEEE Transactions on Circuits and Systems for Video Technology*. 1996; 6(5): 513-518.

[28] Mooser R, Hack E, Sennhauser U, Székely G. Estimation of affine transformations directly from tomographic projections. In: *2009 Proceedings of 6th International Symposium on Image and Signal Processing and Analysis*. Salzburg, Austria: IEEE; 2009. p.377-382.

[29] Mooser R, Forsberg F, Hack E, Székely G, Sennhauser U. Estimation of affine transformations directly from tomographic projections in two and three dimensions. *Machine Vision and Applications*. 2013; 24(2): 419-434.

[30] Nacereddine N, Tabbone S, Ziou D. Similarity transformation parameters recovery based on Radon transform. Application in image registration and object recognition. *Pattern Recognition*. 2015; 48(7): 2227-2240.

[31] Nacereddine N, Tabbone S, Ziou D. Robustness of Radon transform to white additive noise: General case study. *Electronics Letters*. 2014; 50(15): 1063-1065.

[32] Jiangsheng You, Weiguo Lu, Jian Li, Gene Gindi, Zhengrong Liang. Image matching for translation, rotation and uniform scaling by the Radon transform. In: *Proceedings 1998 International Conference on Image Processing. ICIP98 (Cat. No.98CB36269)*. Chicago, IL, USA: IEEE; 1998. p.847-851.

[33] Mao W, Li T, Wink N, Xing L. CT image registration in sinogram space. *Medical Physics*. 2007; 34(9): 3596-3602.
[34] Medan G, Shamul N, Joskowicz L. Sparse 3D radon space rigid registration of CT scans: Method and validation study. *IEEE Transactions on Medical Imaging*. 2016; 36(2): 497-506.
[35] Yan H, Liu J, Sun J. Edge projection-based image registration. In: *Knowledge-Based Intelligent Information and Engineering Systems*. Berlin/Heidelberg, Germany: Springer; 2005. p.1231-1237.
[36] Natterer F. *The Mathematics of Computerized Tomography*. Philadelphia, PA, USA: SIAM; 2001.
[37] Hughes TJR. *The Finite Element Method: Linear Static and Dynamic Finite Element Analysis*. Mineola, NY, USA: Courier Corporation; 2012.
[38] Goodfellow I, Bengio Y, Courville A. *Deep Learning*. Cambridge, MA, USA: MIT Press Cambridge; 2016.
[39] Hurtado DE, Villarroel N, Retamal J, Bugedo G, Bruhn A. Improving the accuracy of registration-based biomechanical analysis: A finite element approach to lung regional strain quantification. *IEEE Transactions on Medical Imaging*. 2016; 35(2): 580-588.
[40] Andrade CI, Hurtado DE. Inelastic deformable image registration (*i*-DIR): Capturing sliding motion through automatic detection of discontinuities. *Mathematics*. 2021; 9(1): 97.
[41] Jafari-Khouzani K, Soltanian-Zadeh H. Rotation-invariant multiresolution texture analysis using radon and wavelet transforms. *IEEE Transactions on Image Processing*. 2005; 14(6): 783-795.
[42] Flusser J. An adaptive method for image registration. *Pattern Recognition*. 1992; 25(1): 45-54.
[43] Haber E, Heldmann S, Modersitzki J. Adaptive mesh refinement for nonparametric image registration. *SIAM Journal on Scientific Computing*. 2008; 30(6): 3012-3027.
[44] Barnafi N, Gatica GN, Hurtado DE, Miranda W, Ruiz-Baier R. Adaptive mesh refinement in deformable image registration: A posteriori error estimates for primal and mixed formulations. *SIAM Journal on Imaging Sciences*. 2021; 14(3): 1238-1272.